Research Article | Vol. 32, No. 12 / 3 Jun 2024 / Optics Express 21216
Optics EXPRESS

Manipulating terahertz guided wave excitation with Fabry-Perot cavity–assisted metasurfaces

YUANDA LUO,[1] WANGCHENG YE,[1] LINJIE ZHOU,[2] AND JINGYA XIE[1,*]

[1]*Terahertz Technology Innovation Research Institute, and Shanghai Key Laboratory of Modern Optical System, University of Shanghai for Science and Technology, No. 516 JunGong Road, Shanghai 200093, China*
[2]*State Key Laboratory of Advanced Optical Communication Systems and Networks, Department of Electronic Engineering, Shanghai Jiao Tong University, Shanghai 200240, China*
[*]*xiejy@usst.edu.cn*

Abstract: Metasurfaces are emerging as powerful tools for manipulating complex light fields, offering enhanced control in free space and on-chip waveguide applications. Their ability to customize refractive indices and dispersion properties opens up new possibilities in light guiding, yet their efficiency in exciting guided waves, particularly through metallic structures, is not fully explored. Here, we present a new method for exciting terahertz (THz) guided waves using Fabry-Perot (FP) cavity-assisted metasurfaces that enable spin-selective directional coupling and mode selection. Our design uses a substrate-free ridge silicon THz waveguide with air cladding and a supporting slab, incorporating placed metallic metasurfaces to exploit their unique interaction with the guided waves. With the silicon thin layer and air serving as an FP cavity, THz waves enter from the bottom of the device, thereby intensifying the impact of the metasurfaces. The inverse-structured complementary metasurface could enhance excitation performance. We demonstrate selective excitation of TE_{00} and TE_{10} modes with directional control, confirmed through simulations and experimental validations using a THz vector network analyzer (VNA) system. This work broadens the potential of metasurfaces for advanced THz waveguide technologies.

1. Introduction

Metasurfaces, the two-dimensional counterparts to metamaterials, have revolutionized the manipulation of electromagnetic waves by imparting local and space-variant phase discontinuities to incident light [1,2]. The advancement of metasurfaces has led to unprecedented control over complex light fields in free space, enabling functionalities such as beam shaping [3,4], focusing [5], optical vortices [6,7], and sensing [8,9], and so on. Extending beyond free-space applications, the integration of metasurfaces within on-chip platforms heralds a new field in photonic integrated circuits (PICs), enticing researchers with the potential for compact, highly functional devices that can guide light with tailored characteristics.

In the domain of PICs, the silicon waveguide platform plays a vital role, relying on its compatibility with complementary metal-oxide-semiconductor (CMOS) processing. It offers attractive on-chip applications, including high-speed optical interconnects [10,11], optical signal processing [12–14], and optical sensing [15,16]. Conventional silicon waveguides can strongly confine light in them due to their high refractive index contrast, but they have limited functionalities and lack complete control over light. Recently, there has been growing interest in introducing subwavelength-structured metasurfaces and metamaterials into silicon waveguides to achieve more flexible control of light [17,18]. As arrays of optical scatterers with subwavelength spacing and engineered geometry, metasurfaces exhibit a high degree of freedom in tailoring the phase and polarization of light [19–23]. Especially, leveraging the strong interaction between metasurfaces and waveguide modes, researchers can apply gradient metasurfaces on waveguide

#525377 https://doi.org/10.1364/OE.525377
Journal © 2024 Received 2 Apr 2024; revised 1 May 2024; accepted 13 May 2024; published 23 May 2024

Optics EXPRESS

surfaces to control the propagation of guided waves [24,25] or to excite guided waves with light propagation in free space [26–36]. Besides, as directional excitation is ubiquitous in photonics, it is highly desired to separate light beams into different directions with well-defined modes depending on their polarization states or wavelengths. The flexibility and configurability of optical antennas can enable novel waveguide couplers with a compact footprint and versatile functionalities. Quite recently, the gradient metasurface was employed to realize directional coupling [30,31,37,38]. Nevertheless, dielectric metasurfaces loaded on waveguides are difficult to fabricate, while metal metasurfaces exhibit low efficiency and substantial ohmic losses in the optical domain. Despite the significant progress in on-chip light manipulation, metasurface's role in PICs requires further exploration and understanding.

In this paper, we present a method for the excitation of THz guided waves, employing the phase gradient attributes offered by metasurfaces. Unlike previous works [26–38], which have demonstrated the potential of metasurfaces in controlling light propagation and waveguide mode excitation, our work contributes to the field by integrating FP cavity-assisted metasurfaces into the devices. This not only demonstrates a versatile technique that allows for spin-selective directional coupling and mode selection, but also harnesses the interplay between the metasurface and an FP cavity to increase efficiency performance. We introduce a ridge silicon THz waveguide, notable for its absence of a substrate, which is mechanically supported by a slab and clad with air. This structure, distinct from conventionally used waveguide structures, forms a three-layer thin film system of air-silicon-air, constituting an FP cavity. The metallic metasurfaces are placed on the top of the waveguide. The silicon, positioned as the middle layer in the FP cavity, facilitates multiple oscillations of incident light and also serves as a THz waveguide. This configuration effectively enhances the interaction between the metasurfaces and the guided waves. Through numerical analysis, we shed light on the crucial role played by the FP cavity-assisted metasurface in the efficiency performance of the device. Furthermore, our numerical findings suggest that employing a complementary metasurface, composed of structures that are the inverse of traditional nanorods and feature subwavelength apertures in a thin metallic film, can lead to enhanced efficiency performance.

We also explore the use of a unidirectional effective wavevector, introduced by a linear spin-dependent gradient phase along the waveguide, to achieve directional guided wave excitation. When incident light is either left-handed circularly polarized (LCP) or right-handed circularly polarized (RCP), the waveguide modes can be excited at the left or right ports, respectively, based on the effective refractive index as derived from Snell's Law. By manipulating the spatial modal overlap between the metasurface's scattering near-field and the waveguide mode of interest, our design enables mode-specific excitation. Supported by our simulations, we have demonstrated selective excitation of TE_{00} and TE_{10} modes with inherent directional control. To corroborate the simulation results, we conducted experimental validation using an electric-field scanning THz VNA system, and the outcomes were consistent with the simulations. Our work paves the way for chip-scale THz innovations, particularly in integrated polarization (de)multiplexers, revealing their potential for robust and precise THz signal management.

2. Fundamentals and design principles

Conventional THz integrated waveguides are based on silicon slabs with air cladding and have a ridged structure, using the slab as a mechanical support without a substrate [39–44]. Taking advantage of this characteristic, we propose a new method to manipulate THz guided wave excitation with FP cavity-assisted metasurfaces for higher efficiency. The three-layer thin film system of air-silicon-air constitutes an FP cavity. The high-refractive index silicon waveguides with a single-layer gold metasurface and air-cladding are shown in Fig. 1(a). To excite and manipulate guided waves inside the dielectric waveguides from free space light, the metasurface is integrated on the top of silicon waveguides. The metasurface is constructed by gold rods

Optics EXPRESS

with a constant gradient of orientation angle θ along the x direction to generate a linear gradient phase. The properly engineered phase gradient is determined by combining generalized Snell's law with phase-matching conditions. By assigning opposite phase gradients to two orthogonal incident polarizations, the propagation direction of the fundamental mode in the waveguide can be flipped by the spin of the incident light. For selective excitation of high-order modes in multimode waveguides, the relative location of the antenna arrays should be judiciously arranged. Considering the spatial mode overlap between gold rods scattering near field and target waveguide mode, the number of gold rod arrays is decided by the order of the modes. For instance, to selectively excite $TE_{m,n}$ mode, m + 1 arrays of gold rods are required.

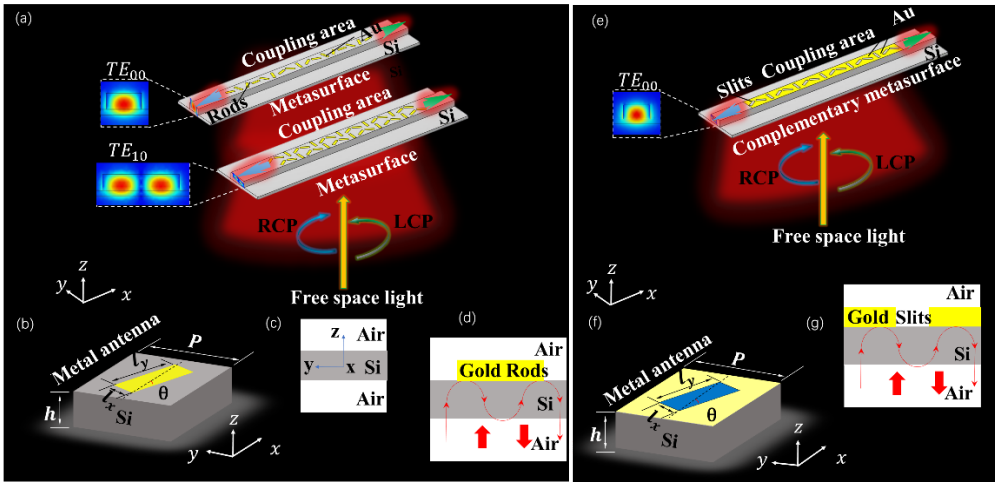

Fig. 1. Schematics of manipulating THz guided wave excitation with FP cavity-assisted metasurface. (a) Schematics of waveguides excited by the gold microrod metasurfaces. (b) The θ-oriented Pancharatnam-Berry (PB) phase meta-unit. (c) Schematics of three layer medium structure of air-silicon-air. (d) Illustration of the meta-unit cross-section with silicon waveguide layer acting as an FP cavity. (e) Schematics of waveguides excited by the complementary geometric metasurfaces for higher efficiency. (f) The θ-oriented complementary meta-unit. (g) Illustration of the cross-section of the complementary meta-unit.

Gold microrods are explored here because they have been crucial in the development of metasurfaces and are well understood as metasurface material represents a nearly perfect conductor in the THz domains. However, these metasurfaces have been limited so far by the low conversion efficiency between the two circular polarization states. As the PB metasurface is shined by a spin-polarized beam, its scatterings generate four beams, which are normal or anomalous modes of transmission or reflection. While the meta-atoms are rotated by an angle θ, the anomalous modes will carry an additional spin-dependent but dispersionless PB phase of $\pm 2\theta$ [45]. The normal modes, in contrast, do not display such a phase shift. Generally, in a reflective PB metasurface, the anomalous mode is spin-conserved and the normal mode is spin-flipped. Conversely, within a transmissive PB metasurface, this behavior is inverted. The following nonlinear equation fundamentally constrains the amplitude of the reflection conversion efficiency R_a [46]

$$|R_a|^2 = Re[R_n] - |R_n|^2 \tag{1}$$

where the subscripts a and n indicate anomalous and normal reflection modes, respectively. From this condition, we see that the amplitude of anomalous reflection is uniquely determined by the

Optics EXPRESS

normal reflection efficiency. The maximum conversion efficiency is 0.25, when R_n is equal to 0.5 [46]. The amplitude of the transmission conversion efficiency T_a has a similar form.

We start from analyzing the electromagnetic properties of the building block (meta-unit) of our metasurfaces in Fig. 1(b). This configuration maintains very large reflection amplitudes for anomalous mode light, which forms the basis of the high-efficiency geometric metasurfaces for manipulating THz guided wave excitation. The higher efficiency conversion arises from the FP effect of three-layer thin film system of air-silicon-air as shown in Fig. 1(c). In our case, $n_1 = 1$ (air) and $n_3 = 3.42$ (silicon). The configuration of the entire device is the sheet of antennas on top of a finite thick silicon layer with an air cladding. If the light is incident from the top, then the transmitted signal of metasurfaces needs to be coupled to the waveguide; if it is incident from the bottom, the reflected signal of metasurfaces is coupled to the waveguide instead as shown in Fig. 1(d). Due to the large reflection coefficient of gold microrod, the reflection mode of light incident from the bottom surface is more efficient. To further enhance the advantages of this structure and increase reflectivity, a complementary unit structure can be used, as shown in Figs. 1(e)-1(g). With a higher proportion of metal, the reflection coefficient of this structure is further increased, which can enhance the conversion efficiency even more.

To construct the waveguide-integrated metasurface, we designed a metallic building block that can act as an imperfect half-wave plate. The 0.15 μm-thick metal antenna unit is deposited on a Si layer with a thickness of 150 μm which is consistent with the silicon waveguide height to be designed next. The length, width, and square lattice period of metal antenna, namely *lx*, *ly,* and *P* are shown in Fig. 1(b). We set $\theta = 0°$, $lx = 40$ μm, $ly = 145$ μm, and $P = 170$ μm. Periodic boundaries are applied to the x and y directions. Then the simulated transmission and reflection efficiencies with normal light incidence from the top are shown in Fig. 2(a). Generally, both the transmitted and reflected waves comprise circular polarization states that can be categorized into either normal or anomalous modes of transmission and reflection. The transmission of the anomalous mode under such conditions of light incidence is only 15% around 0.3 THz, as indicated by the pink dashed curve. In a contrasting scenario, as depicted by the orange solid curve in Fig. 2(b), simulations for light incident from the bottom show that the reflectivity of anomalous mode exceeds 70% around 0.41 THz. This reflectivity is significantly higher than the aforementioned transmission efficiency and surpasses the theoretical maximum of 0.25, as outlined in Eq. (1). For the complementary meta-unit, the gold rods are replaced with slits in a thin film of gold, as shown in Fig. 1(f). Numerical simulation results show that the metasurface can improve the device's conversion efficiency performance more. The reflectivity of anomalous mode is over 81% around 0.44 THz, as shown by the orange solid curve in Fig. 2(c), which is even higher. In order to further verify the FP cavity effect formed by the finite thickness silicon layer sandwiched between metasurface and air, we simulated the conversion efficiency of the same meta-unit, keeping all design parameters constant except for the thickness of the silicon layer, which was varied. The results are shown in Fig. 2(d). For different silicon thicknesses, the frequency corresponding to the maximum conversion efficiency varies, and the variation period of the spectra is also affected. Therefore, the results show that the multilayer structure is different from ordinary metasurface devices, and it has a superimposed FP effect. Figure 2(e) shows the geometric phase variation of normal and anomalous mode reflected waves as a function of the orientation angle for both conventional and complementary metasurfaces under normal light incidence from the bottom of the device. The operating frequency for the conventional metasurfaces is 0.41 THz, while the complementary metasurfaces function at 0.45 THz.

We then designed the THz silicon ridge-type waveguides, where TE single-mode and high-order modes can propagate around 0.5 THz. Figure 2(f) shows the cross-sectional view of the waveguide. The ridge waveguide is 110 μm-high with a 40 μm-thick slab. To demonstrate the principle of our device, we designed two TE modes in the waveguides. The waveguide widths are selected as 220 μm and 320 μm for the TE_{00} and TE_{10} mode, respectively. The electric field norm

Optics EXPRESS

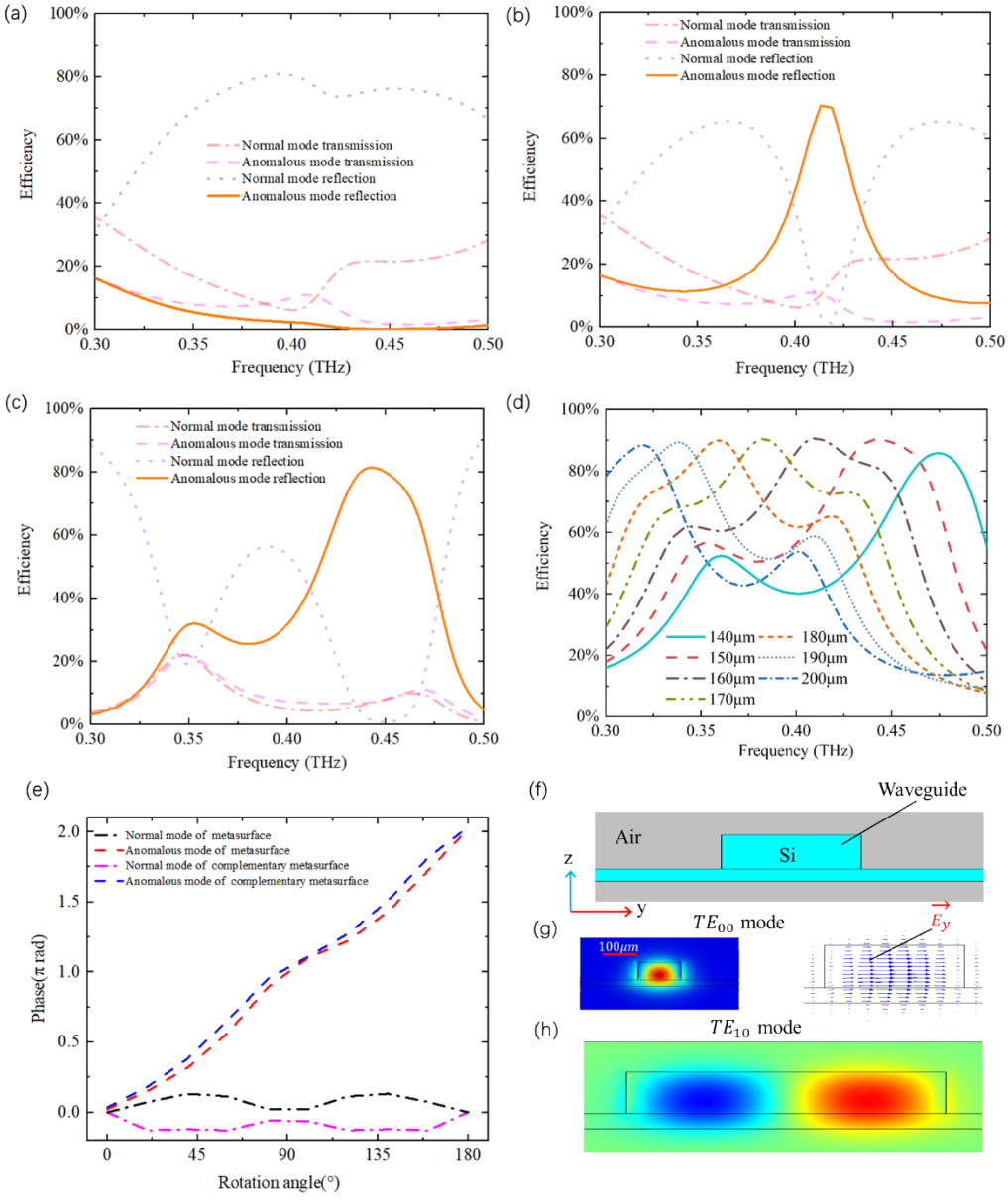

Fig. 2. Simulated transmission and reflection with normal light incidence from (a) the top and (b) the bottom of a uniform metasurface with all antennas aligned along the same direction. (c) Simulated transmission and reflection with normal light incidence from the bottom of a uniform complementary metasurface. (d) The simulated anomalous mode reflection of complementary metasurface with different silicon layer thicknesses. (e) The PB geometric phase variation of the normal and anomalous mode reflected wave, as a function of the orientation angle of the conventional and complementary meta-units with normal light incidence from the device bottom. (f) Schematic of the cross-sectional view of the THz ridge-waveguide. (g) **|E|** distribution and vector diagram of the TE_{00} mode, respectively. (h) Electric field component (**Ey**) distribution for the TE_{10} mode.

Optics EXPRESS

|E| distribution of fundamental TE_{00} mode is shown in Fig. 2(g). We also plot the corresponding vector diagrams. The dominant electric field component of the TE mode is *y*-polarized. In order to better present the phase characteristic, the dominant electric field component distribution of high-order mode TE_{10} ($\mathbf{E_y}$) is shown in Fig. 2(h). We note that for the high-order modes, a phase difference of π exists between adjacent mode lobes. The mode calculation here to obtain the effective refractive index and field distribution is very important for controlling the launching of specific modes.

The metasurface is then deposited on top of this silicon waveguide, which locally encodes a configurable and polarization-dependent phase to incident electromagnetic waves. The antennas with the same geometry but different rotation angles are used to apply opposite phase profiles to two circular polarizations. The gradient phase generated by the metasurface should offer a wavevector match between the normal incidence and the guide mode in the silicon waveguide. This condition can be described as general Snell's law [24]

$$n_{eff} = \frac{\lambda_0}{2\pi}\frac{\Delta\varphi}{P} \cdot sign\left(\frac{\Delta\varphi}{P}\right) \tag{2}$$

where $\Delta\varphi$ is the constant phase difference between two adjacent antennas along the x-axis. The excitation direction is determined by the sign of phase gradient, which can be controlled by the spin of the incident light. The effective refractive index n_{eff} of silicon waveguides can be obtained by the mode calculation, and the lattice period P can be optimized. Consequently, the constant phase difference $\Delta\varphi$ can be achieved to satisfy the phase-matching condition. If the rotation angle of the middle metal antenna is set to 0 degrees, then the rotation angle of each antenna can be determined through the constant phase difference. Compared with the metasurfaces composed of thousands of meta-atoms and even more for electromagnetic manipulation in free space, the number of the meta-atoms of chip-integrated metasurface can be greatly reduced to a few. Since only the components of anomalous mode can be coupled into the silicon waveguide while those of normal mode without phase modulation are transmitted through or directly reflected, the conversion efficiency of the geometric metasurface is a significant factor that determining the excitation efficiency of the designed device.

3. Methods

For the experimental demonstration, the fabrication process of waveguides hybridized with geometric metasurfaces was conducted on a 2-inch high-resistivity silicon wafer with a thickness of 150 μm. The silicon wafer was first doposited with a 150-nm-thick gold (Au) film using a gold sputter coater. Following metallization, optical lithography was performed on the Au film. The Au film was then etched using ion beam etching (IBE) to form the metallic antennas on the silicon surface. This step defined the geometric metasurface structures. A second round of optical lithography was conducted to define the waveguides directly beneath the metasurface structures with precise alignment. The wafer was then etched to a depth of 110 μm using the deep reactive ion etching (DRIE) process to form the waveguides. Finally, the samples were cut perpendicular to the output ports of the waveguides in preparation for measurement.

4. Results and discussions

The performance of our devices has been evaluated through both numerical simulations and experiments. Figures 3(a) and 3(b) show the schematic and microscope image of the fabricated device, respectively. This device is capable of directionally exciting THz guided waves into the right or left port of the waveguide for the TE_{00} mode, under the illumination of LCP or RCP waves. The orientation angle difference between two adjacent antennas is 125.45°. The antenna array is positioned at the waveguide's center to optimize spatial modal overlap with the

Optics EXPRESS

fundamental mode. For this demonstration, we employed 17 antennas to illustrate the principle of directional excitation. It is noteworthy that for an incident THz beam with a large spot size, the power coupled into the waveguide increases with the number of antennas used. Figures 3(c) and 3(d) display the electric field intensity distributions, $|\boldsymbol{E}_y|^2$, in the x-y plane bisecting the waveguide for LCP and RCP incident light at 0.4822 THz. The observed deviation of the device's operational frequency from the values presented in Fig. 2 may originate from the utilization of the waveguide's effective refractive index in Snell's law phase calculations. Re-evaluating this with the effective refractive index of the hybrid waveguide, which incorporates gold antennas, is expected to increase the precision of the frequency estimation. For LCP normal incidence, a waveguide mode is excited and routed to the + x direction, while the power coupled to the left side is negligible. When the chirality of the incident light is reversed, the direction of the light coupling into the waveguide is also reversed.

We fabricated the device and investigated its characteristics using a THz VNA system, as shown in Fig. 3(e). This system comprises an Agilent N5227A PNA network analyzer and a set of WR-2.2 325-500 GHz frequency extenders. A transmitting horn antenna is directly connected to one frequency extender, while a near-field probe waveguide is connected to the other extender. The antenna emits THz waves, which are then collimated through a parabolic mirror. These waves are converted into circularly polarized THz waves via a quarter-wave plate before being incident perpendicularly onto the slab side of the waveguide. The diameter of the beam spot on the waveguide upon THz wave illumination is approximately 4 mm. The probe is placed next to the end of the silicon waveguide to serve as the receiver. Given that the waveguide's evanescent field extends on the scale of hundreds of micrometers and the device's scanning range is on a centimeter scale, maintaining precise control over the distance between the probe and the waveguide within the evanescent field range presents a significant challenge due to the limitations of the current system's positional accuracy. As a result, our experiments employ a method of scanning the output light spot from the waveguide port to demonstrate the functionality of directional excitation. We obtain the electric field amplitude and phase distributions by moving the probe step-by-step along the y and z directions. The movement of the near-field probe has a resolution of 100 μm.

Figure 3(f) presents the experimental electric field intensity distribution, $|\boldsymbol{E}_y|^2$, (the y-z-cross-section) of the waveguide's left port for RCP incident light, with a scanning area of 4 mm × 4 mm. The device operates in the TE_{00} mode at 0.49 THz. The desired modes are excited, aligning well with the theoretical analysis. When we adjust the quarter-wave plate to achieve LCP incidence, the output electric field intensity of this port is almost without signal, as shown in Fig. 3(g). To quantitatively characterize the performance of directional excitation, we use the simulated and experimental excitation spectra corresponding to the light output from the waveguide port. We retrieved the simulation s-parameters of the left port for the two circularly polarized incident lights as a function of frequency, as shown in Fig. 3(h). The red line indicates the directional excitation spectra under RCP illumination. The maximum efficiency is 4.6% at 0.482 THz. Limited by computational resources, the efficiency has not been optimized. In reality, by optimizing the parameters of the entire waveguide structure, it is possible to improve the congruence between the frequency of wavevector matching and the frequency at which the metasurface achieves maximum efficiency, thereby enhancing the operational efficiency of the final device. The black curve represents LCP irradiation, which shows virtually no energy output over the entire spectrum range. In the experimental results, the maximum directional waveguide excitation can be realized around 0.498 THz, as shown by the red curve in Fig. 3(i). Similarly, the black curve represents the LCP irradiation, which shows virtually no energy output over the entire spectrum range. The detected power at each frequency is normalized to the maximum power of the RCP illumination condition. There is a noticeable shift of 0.016 THz in the maximum frequency compared to the simulation results. The shift in the operational frequency band could

Optics EXPRESS

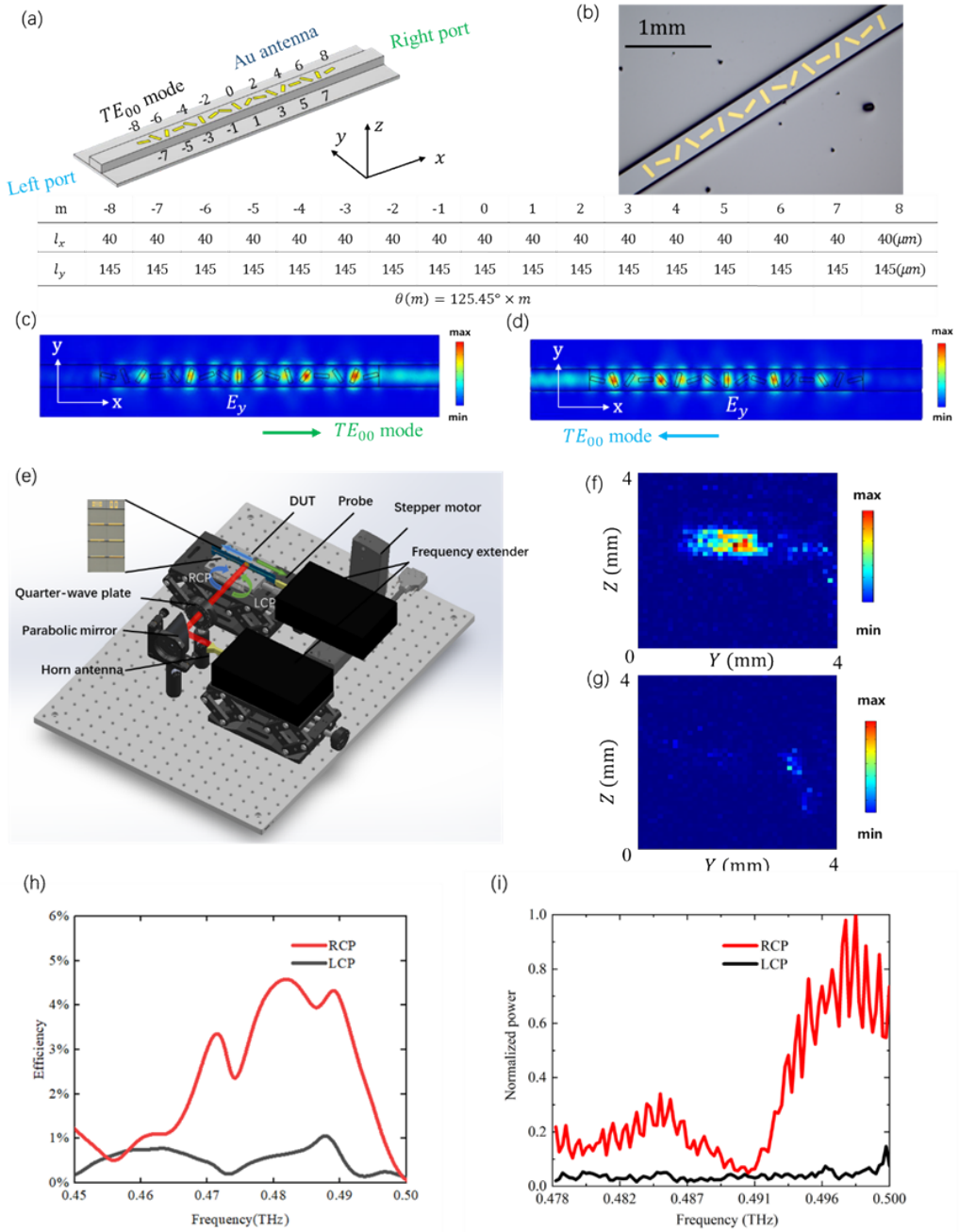

m	-8	-7	-6	-5	-4	-3	-2	-1	0	1	2	3	4	5	6	7	8
l_x	40	40	40	40	40	40	40	40	40	40	40	40	40	40	40	40	40(μm)
l_y	145	145	145	145	145	145	145	145	145	145	145	145	145	145	145	145	145(μm)

$$\theta(m) = 125.45° \times m$$

Fig. 3. (a) Schematic and (b) microscopic image of the fabricated device, which can directionally excite THz guided waves into the right or left port of the waveguide for the TE_{00} mode under the illumination of LCP or RCP waves, respectively. (c)(d) Electric field intensity distributions, $|\boldsymbol{E_y}|^2$, in the x-y plane bisecting the waveguide for LCP and RCP incident light at 0.4822 THz. (e) Experimental setup of the electric-field scanning THz VNA. (f)(g) Experimental electric field intensity distribution $|\boldsymbol{E_y}|^2$ of the waveguide's left port (the y-z-cross-section) for RCP and LCP incident light, respectively. (h)(i) Simulated and normalized experimental spectra of the left port for the two circularly polarized incident lights.

Optics EXPRESS

be due to the fabrication errors of the device. As seen in Fig. 2(d), the thickness of the silicon waveguide can cause a resonance shift in the FP cavity. This indicates that variations in the initial thickness of the wafer can lead to discrepancies in the performance of the device at frequencies. Additionally, inaccuracies in the etching depth of the silicon, as well as dimensional errors in the metal structures, can also have an impact on the final efficiency of the device. These factors will be considered in the future work to further optimize the design and fabrication process.

To further demonstrate waveguide mode-configurable excitation, a properly engineered spatial overlap is necessary, as indicated by the higher-order mode calculation in Fig. 2. For the second-order TE_{10} mode, two rows of antennas (with an interval of $\Delta y = 160\mu m$) can achieve superior electric field overlap. Given that a phase difference of π exists between adjacent mode lobes, the adjacent antenna arrays should be spatially dislocated by half of the mode period. Figures 4(a) and 4(b) present the schematic and microscopic image of the fabricated device, respectively. The waveguide width is 320μm. Based on the effective refractive index for the TE_{10} mode, we set the phase step to $\Delta\varphi_{TE10} = \pm 238.88°$. Consequently, the rotation angle difference of adjacent antennas is half of the phase step, $\pm 119.44°$. Because a phase difference exists between the two mode lobes for the TE_{10}, we spatially dislocate the two antenna rows by $\Delta x = \lambda/(2n_{eff})$ along the x-direction. This ensures the electric field scattered by the two antenna arrays is π out of phase.

Figures 4(c) and 4(d) display the electric field intensity distributions $|\boldsymbol{E_y}|^2$ in the x-y plane bisecting the waveguide under LCP and RCP incidence at 0.4878 THz, respectively. The results demonstrate similar directional coupling and the excitation of the required TE_{10} mode. Similarly, the electric field intensity and phase distribution of the right waveguide port were experimentally tested, as shown in Figs. 4(e) and 4(f). For the LCP condition, the TE_{10} mode is excited, while for the RCP condition, there is virtually no energy output. Notably, the phase difference between the energy positions of the two lobes of the mode is almost π as shown in Fig. 4(g), which aligns with the theoretical expectation, further validating the successful excitation of the TE_{10} mode in the experiment. The simulated s-parameters of the right port for the two circularly polarized incident lights as a function of frequency are shown in Fig. 4(h). The red line indicates the excitation spectrum under LCP illumination, with a maximum efficiency of 7.4%. In our device, due to its finite width and edge scattering, superior excitation efficiency in higher-order modes is achieved through their larger waveguide width and metasurface area. However, the excitation spectrum under RCP illumination also shows an increase at this port, as indicated by the black curve. Therefore, defining mode excitation contrast ratio as $10 \times \log_{10}(T_{LCP}/T_{RCP})$, where T_{LCP} and T_{RCP} correspond to the transmissions under LCP and RCP illumination, respectively, it becomes apparent that the contrast ratio introduced by the two circularly polarized lights in this device fails to demonstrate a marked enhancement. In the experimental results, the transmissions are normalized to the maximum power of the LCP illumination condition, as shown in Fig. 4(i). The peak of directional waveguide excitation can be achieved around 0.49 THz. For the second-order TE_{10} mode, the port excitation power surpasses that of the fundamental mode in silicon waveguides.

We also design the complementary structure of the original antenna as an alternative basic unit of the metasurfaces. The schematic and microscope images of the fabricated device are shown in Figs. 5(a) and 5(b). The silicon waveguides integrated with complementary geometric metasurfaces share the same operation principle as the previous devices but can exhibit higher excitation directivity. Numerical simulations and experiments are conducted to demonstrate the superior performance of devices with complementary metasurfaces. The parameters of the complementary metallic slit are P=170μm, $l_x = 40\mu m$, $l_y = 145\mu m$. The silicon waveguide structure remains the same as before. Similarly, the general Snell's law is utilized to obtain the phase difference Δφ, so the rotation angle of slit antennas can be determined. The slit antennas

Optics EXPRESS

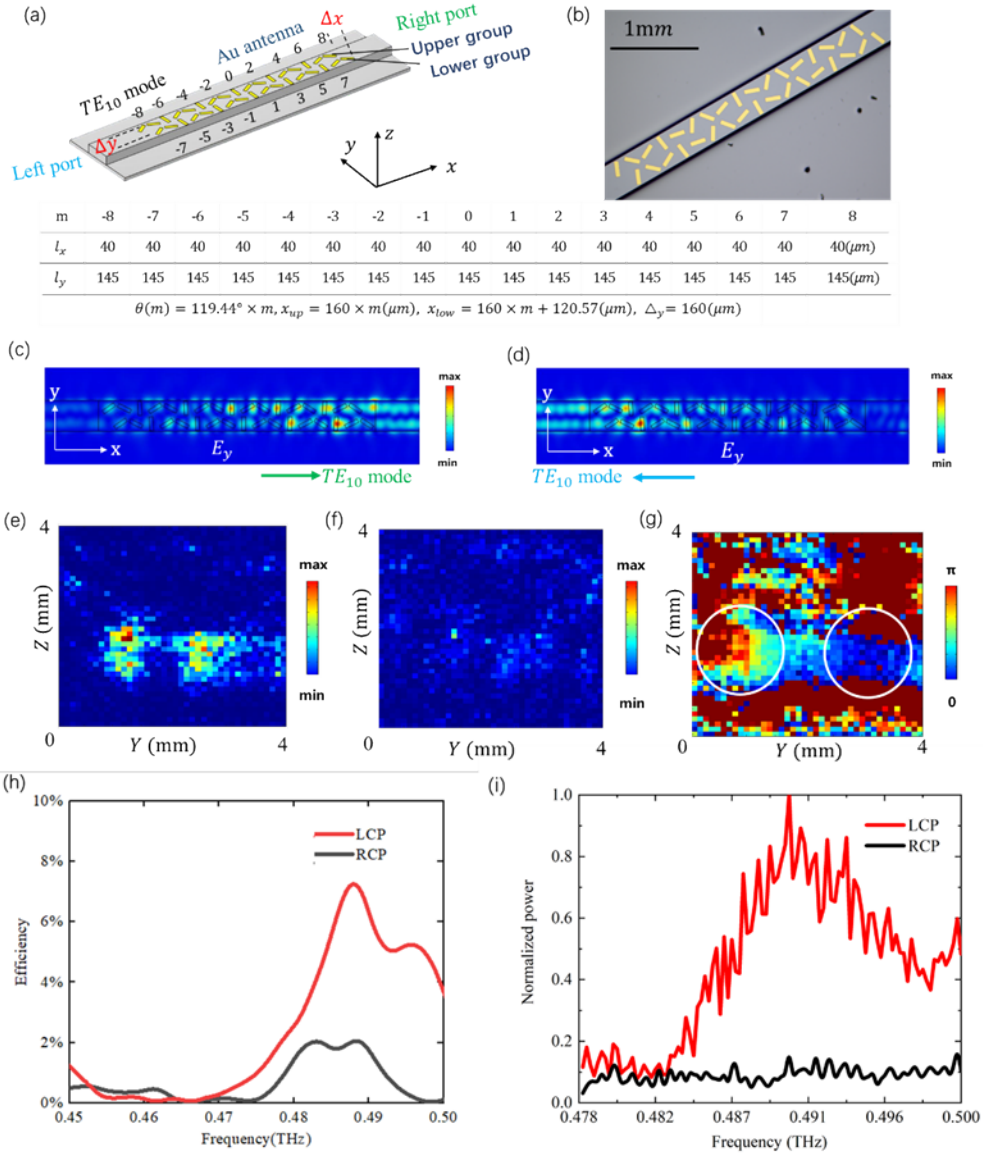

m	-8	-7	-6	-5	-4	-3	-2	-1	0	1	2	3	4	5	6	7	8
l_x	40	40	40	40	40	40	40	40	40	40	40	40	40	40	40	40	40(μm)
l_y	145	145	145	145	145	145	145	145	145	145	145	145	145	145	145	145	145(μm)

$\theta(m) = 119.44° \times m, x_{up} = 160 \times m(\mu m),\ x_{low} = 160 \times m + 120.57(\mu m),\ \triangle_y = 160(\mu m)$

Fig. 4. (a) Schematic and (b) microscopic image of the fabricated device, which can directionally excite THz guided waves into the right or left port of the waveguide for the TE_{10} mode with two rows of dislocated antennas (upper and lower groups), respectively. (c)(d) $|\boldsymbol{E_y}|^2$ distributions in the x-y plane bisecting the waveguide under LCP and RCP wave illumination (f = 0.4878 THz), respectively. (e)(f) $|\boldsymbol{E_y}|^2$ distributions at the right waveguide port under LCP and RCP incidence, respectively. (g) Phase of the electric field at the right port under LCP incidence. (h)(i) Simulated and normalized experimental spectra of the right port for the two circularly polarized incident lights.

are located at the center of the waveguide to maximize spatial modal overlap with the fundamental mode.

The electric field intensity distributions $|\boldsymbol{E_y}|^2$ in the x-y plane bisecting the waveguide for LCP and RCP incidence light at 0.478 THz are shown in Figs. 5(c) and 5(d), respectively. For

Optics EXPRESS

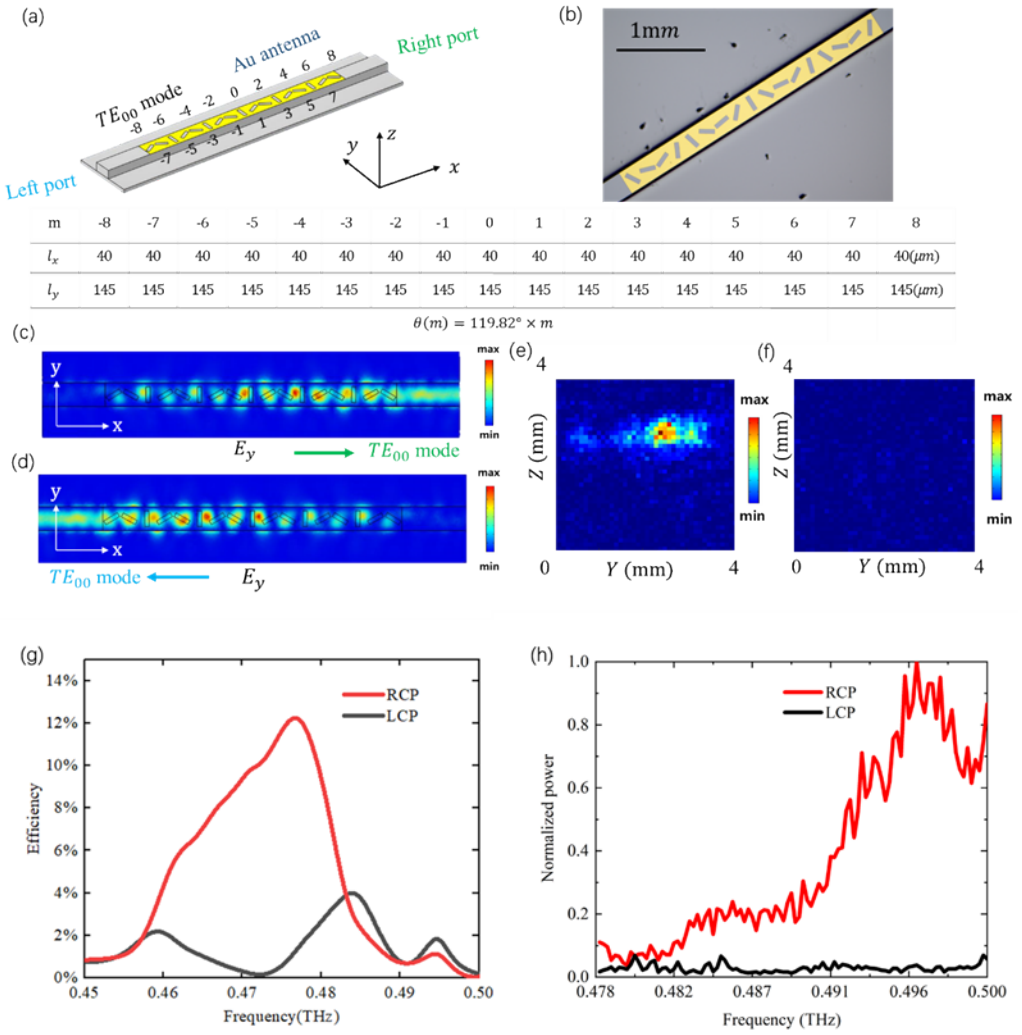

m	-8	-7	-6	-5	-4	-3	-2	-1	0	1	2	3	4	5	6	7	8
l_x	40	40	40	40	40	40	40	40	40	40	40	40	40	40	40	40	40(μm)
l_y	145	145	145	145	145	145	145	145	145	145	145	145	145	145	145	145	145(μm)

$$\theta(m) = 119.82° \times m$$

Fig. 5. (a) Schematic and (b) microscopic image of the fabricated device using complementary metasurfaces for the TE_{00} mode. (c)(d) $|\boldsymbol{E_y}|^2$ distributions in the x-y plane bisecting the waveguide under LCP and RCP wave illumination (f = 0.478 THz), respectively. (e)(f) $|\boldsymbol{E_y}|^2$ distributions at the left waveguide port under RCP and LCP incidence, respectively. (g)(h) Simulated and normalized experimental spectra of the left port for the two circularly polarized incident lights.

LCP normal incidence, a waveguide mode is excited and routed to the + x direction while the power coupled to the left side can be nearly neglected. However, when the chirality of the incident light is reversed, the light coupling into the waveguide flips to the opposite direction. In the experiments, Fig. 5(e) shows the output electric field intensity distribution $|\boldsymbol{E_y}|^2$ of the left waveguide port at 0.49 THz for the TE_{00} mode under RCP incidence, with a scanning area of 4 mm × 4 mm. The results closely match the desired cross-sectional field distributions. When we adjust the quarter-wave plate to achieve LCP incidence, the output electric field intensity of this port is almost without signal, as shown in Fig. 5(f).

We retrieve the simulated s-parameters of the left port for the two circularly polarized incident lights, as shown in Fig. 5(g). The red line indicates the excitation spectra under RCP

Optics EXPRESS

illumination. The maximum efficiency is 12.4% at 0.477 GHz. The black curve represents the LCP irradiation, with virtually no energy output over the designed spectrum range. This suggests that complementary excitation offers higher efficiency and better directionality. In the experimental results, the transmissions are normalized to the maximum power of the RCP illumination condition. The maximum directional waveguide excitation can be realized around 0.497 THz, as shown by the red curve in Fig. 5(h). Similarly, the black curve represents the LCP irradiation, with virtually no energy output over the entire spectrum range. For fundamental mode excitation, silicon waveguides incorporating complementary metasurfaces demonstrate superior performance compared to those with conventional metasurfaces. They not only exhibit higher port excitation power, but also improved directional performance, the latter being evidenced by the lower normalized power values of the black spectral lines in our experiments.

In our devices, the geometric metasurface comprises some antennas with variable spatial orientation. The discrete geometry results in a discontinuous phase profile, introducing phase noise to the scattering fields. However, recent advancements propose continuously shaped geometric metasurfaces composed of catenary structures [47]. We anticipate potential enhancements in our devices, such as using these new metasurfaces to further improve device performance. Moreover, the efficiency of THz guided wave excitation currently remains suboptimal. A predominant factor contributing to this low efficiency is the large THz beam spot size, resulting in only a small portion of the incident THz energy being effectively utilized by the device. A common solution in integrated grating coupler is to employ a taper to broaden the waveguide's width at the grating location, aligning the mode size with the incoming light, thereby boosting coupling efficiency [48]. Similarly, we could improve THz excitation efficiency by enlarging the width of the metasurface's input section, aligning it better with the THz beam spot size. However, this enhancement process necessitates a trade-off between device efficiency and size.

5. Conclusion

In summary, our study has successfully demonstrated a novel application of metasurfaces in the efficient excitation of THz guided waves, particularly through the use of FP cavity-assisted metasurfaces. Our innovative design, which leverages the absence of a substrate in the ridge silicon THz waveguide, not only provides mechanical support through a slab but also effectively utilizes the FP effect to intensify the influence of metasurfaces. A series of devices were numerically and experimentally demonstrated to have desired directional excitation and selected modes by engineering spatial modal overlap. We also presented another waveguide integrated with complementary geometric metasurfaces. Both numerical and experimental results validate that these devices exhibit superior directivity performance. The findings underscore the key role of FP cavity-assisted metasurfaces using thin-film interference effect in the development of advanced THz guided wave excitation devices. Due to the simplicity of the design and its powerful control over guided wave excitation, this flexible method may find practical applications in THz polarization (de)multiplexers, versatile waveguide couplers, and configurable switches for integrated circuits.

Funding. National Natural Science Foundation of China (62275155, 61988102).

Disclosures. The authors declare no conflicts of interest.

Data availability. Data that support the findings of this study are available from the corresponding author upon reasonable request.

References

1. L. Zhang, S. Mei, K. Huang, *et al.*, "Advances in Full Control of Electromagnetic Waves with Metasurfaces," Adv. Opt. Mater. **4**(818), 818 (2016).
2. X. Zang, B. Yao, L. Chen, *et al.*, "Metasurfaces for manipulating terahertz waves," Light Adv. Manuf. **2**(2), 148 (2021).

Optics EXPRESS

3. X. Fu, F. Yang, C. Liu, *et al.*, "Terahertz Beam Steering Technologies: From Phased Arrays to Field-Programmable Metasurfaces," Adv. Opt. Mater. **8**(3), 1900628 (2020).
4. K. Shay, M. Lior, S. Haim, *et al.*, "Shaping light with nonlinear metasurfaces," Adv. Opt. Photonics **10**, 309 (2018).
5. X. Zang, H. Ding, Y. Intaravanne, *et al.*, "A Multi-Foci Metalens with Polarization-Rotated Focal Points," Laser & Photonics Rev. **13**(12), 1900182 (2019).
6. H. Ahmed, H. Kim, Y. Zhang, *et al.*, "Optical metasurfaces for generating and manipulating optical vortex beams," J. Nanophotonics **11**(5), 941–956 (2022).
7. X. Wang, Z. Nie, Y. Liang, *et al.*, "Recent advances on optical vortex generation," J. Nanophotonics **7**(9), 1533–1556 (2018).
8. J. Lyu, S. Shen, L. Chen, *et al.*, "Frequency selective fingerprint sensor: the Terahertz unity platform for broadband chiral enantiomers multiplexed signals and narrowband molecular AIT enhancement," PhotoniX **4**(1), 28 (2023).
9. J. Lyu, L. Huang, L. Chen, *et al.*, "Review on the terahertz metasensor: from featureless refractive index sensing to molecular identification," Photonics Res. **12**(2), 194–217 (2024).
10. D.A.B. Miller, "Optical interconnects to silicon," IEEE J. Select. Topics Quantum Electron. **6**(6), 1312–1317 (2000).
11. J.K. Doylend and A.P. Knights, "The evolution of silicon photonics as an enabling technology for optical interconnection," Laser & Photonics Rev. **6**(4), 504–525 (2012).
12. W. Zhang and J. Yao, "A fully reconfigurable waveguide Bragg grating for programmable photonic signal processing," Nat. Commun. **9**(1), 1396 (2018).
13. J Wang and Y. Long, "On-chip silicon photonic signaling and processing: a review," Sci. Bull. **63**(19), 1267–1310 (2018).
14. M. Chen, H. Yu, and J. Wang, "Silicon Photonics-Based Signal Processing for Microwave Photonic Frontends," in *Silicon Photonics III: Systems and Applications* (Springer, 2016).
15. Y. Chen, H. Lin, J. Hu, *et al.*, "Heterogeneously Integrated Silicon Photonics for the Mid-Infrared and Spectroscopic Sensing," ACS Nano **8**(7), 6955–6961 (2014).
16. M. Sreenath, A.M. George, and K.A. Ansal, "State of the art Sensing Techniques using Silicon Photonics," in *International Conference on Circuits and Systems in Digital Enterprise Technology* (2018).
17. Y. Meng, Y. Chen, L. Lu, *et al.*, "Optical meta-waveguides for integrated photonics and beyond," Light: Sci. Appl. **10**(1), 235 (2021).
18. S. Molesky, Z. Lin, A. Y. Piggott, *et al.*, "Inverse design in nanophotonics," Nat. Photonics **12**(11), 659–670 (2018).
19. N. Yu, P. Genevet, M. A. Kats, *et al.*, "Light Propagation with Phase Discontinuities: Generalized Laws of Reflection and Refraction," Science **334**(6054), 333–337 (2011).
20. M. Khorasaninejad and F. Capasso, "Metalenses: Versatile multifunctional photonic components," Science **358**(6367), 6367 (2017).
21. A.V. Kildishev, A. Boltasseva, and V.M. Shalaev, "Planar Photonics with Metasurfaces," Science **339**(6125), 6125 (2013).
22. N. Yu and F. Capasso, "Flat optics with designer metasurfaces," Nat. Mater. **13**(2), 139–150 (2014).
23. A. Arbabi, Y. Horie, M. Bagheri, *et al.*, "Dielectric metasurfaces for complete control of phase and polarization with subwavelength spatial resolution and high transmission," Nat. Nanotechnol. **10**(11), 937–943 (2015).
24. Z. Li, M. Kim, C. Wang, *et al.*, "Controlling propagation and coupling of waveguide modes using phase-gradient metasurfaces," Nat. Nanotechnol. **12**(7), 675–683 (2017).
25. C. Wang, Z. Li, M. Kim, *et al.*, "Metasurface-assisted phase-matching-free second harmonic generation in lithium niobate waveguides," Nat. Commun. **8**(1), 2098 (2017).
26. R. Guo, M. Decker, F. Setzpfandt, *et al.*, "High–bit rate ultra-compact light routing with mode-selective on-chip nanoantennas," Sci. Adv. **3**(7), e1700007 (2017).
27. R. Guo, M. Decker, F. Setzpfandt, *et al.*, "Plasmonic Fano Nanoantennas for On-Chip Separation of Wavelength-Encoded Optical Signals," Nano Lett. **15**(5), 3324–3328 (2015).
28. Y. Meng, F. Hu, Y. Shen, *et al.*, "Ultracompact Graphene-Assisted Tunable Waveguide Couplers with High Directivity and Mode Selectivity," Sci. Rep. **8**(1), 13362 (2018).
29. C. Gong, J. Zhang, and S. He, "Hybrid unidirectional meta-coupler for vertical incidence to a high-refractive-index waveguide in telecom wavelength," Opt. Lett. **42**(24), 5098 (2017).
30. Y. Guo, Y. Pu, X. Li, *et al.*, "Chip-Integrated Geometric Metasurface As a Novel Platform for Directional Coupling and Polarization Sorting by Spin–Orbit Interaction," IEEE J. Select. Topics Quantum Electron. **24**(6), 1–7 (2018).
31. Y. Meng, F. Hu, Z. Liu, *et al.*, "Chip-integrated metasurface for versatile and multi-wavelength control of light couplings with independent phase and arbitrary polarization," Opt. Express **27**(12), 16425 (2019).
32. F. B. Arango, A. Kwadrin, and A.F. Koenderink, "Plasmonic Antennas Hybridized with Dielectric Waveguides," ACS Nano **6**(11), 10156–10167 (2012).
33. T. P.H. Sidiropoulos, M.P. Nielsen, T.R. Roschuk, *et al.*, "Compact Optical Antenna Coupler for Silicon Photonics Characterized by Third-Harmonic Generation," ACS Photonics **1**(10), 912–916 (2014).
34. D. Vercruysse, P. Neutens, L. Lagae, *et al.*, "Single Asymmetric Plasmonic Antenna as a Directional Coupler to a Dielectric Waveguide," ACS Photonics **4**(6), 1398–1402 (2017).
35. H. Huang, A.C. Overvig, Y. Xu, *et al.*, "Leaky-wave metasurfaces for integrated photonics," Nat. Nanotechnol. **18**(6), 580–588 (2023).

Optics EXPRESS

36. T. He, Y. Meng, Z. Liu, *et al.*, "Guided mode meta-optics: metasurface-dressed waveguides for arbitrary mode couplers and on-chip OAM emitters with a configurable topological charge," Opt. Express **29**(24), 39406–39418 (2021).
37. Y. Meng, Z. Liu, Z. Xie, *et al.*, "Versatile on-chip light coupling and (de)multiplexing from arbitrary polarizations to controlled waveguide modes using an integrated dielectric metasurface," Photonics Res. **8**(4), 564 (2020).
38. Y. Zhang, Z. Li, W. Liu, *et al.*, "Spin-Selective and Wavelength-Selective Demultiplexing Based on Waveguide-Integrated All-Dielectric Metasurfaces," Adv. Opt. Mater. **7**(6), 1801273 (2019).
39. A. Malekabadi, S. A. Charlebois, D. Deslandes, *et al.*, "High-Resistivity Silicon Dielectric Ribbon Waveguide for Single-Mode Low-Loss Propagation at F/G-Bands," IEEE Trans. THz Sci. Technol. **4**(4), 447–453 (2014).
40. Z. Wang, S. Yuan, G. Dong, *et al.*, "On-chip single-mode high-Q terahertz whispering gallery mode resonator," Opt. Lett. **44**(11), 2835 (2019).
41. J. Xie, X. Zhu, X. Zang, *et al.*, "Terahertz integrated device: high-Q silicon dielectric resonators," Opt. Mater. Express **8**(1), 50 (2018).
42. J. Xie, X. Zhu, H. Zhang, *et al.*, "Terahertz-frequency temporal differentiator enabled by a high-Q resonator," Opt. Express **28**(6), 7898 (2020).
43. H. Zhang, C. Liang, J. Song, *et al.*, "Terahertz out-of-plane coupler based on compact spot-size converter," Chin. Opt. Lett. **20**(2), 021301 (2022).
44. J. Xie, J. Qian, T. Wang, *et al.*, "Integrated terahertz vortex beam emitter for rotating target detection," Adv. Photonics **5**(06), 066002 (2023).
45. Y. Qiu, S. Tang, T. Cai, *et al.*, "Fundamentals and applications of spin-decoupled Pancharatnam-Berry metasurfaces," Front. Optoelectron. **14**(2), 134–147 (2021).
46. X. Ding, F. Monticone, K. Zhang, *et al.*, "Ultrathin Pancharatnam–Berry Metasurface with Maximal Cross-Polarization Efficiency," Adv. Mater. **27**(7), 1195–1200 (2015).
47. M. Pu, X. Li, X. Ma, *et al.*, "Catenary optics for achromatic generation of perfect optical angular momentum," Sci. Adv. **1**(9), e1500396 (2015).
48. L. Cheng, S. Mao, Z. Li, *et al.*, "Grating Couplers on Silicon Photonics: Design Principles, Emerging Trends and Practical Issues," Micromachines **11**(7), 666 (2020).